*Article*

# NMR Structure and Biophysical Characterization of Thermophilic Single-Stranded DNA Binding Protein from *Sulfolobus Solfataricus*

**Min June Yang [1]**, **Jinwoo Kim [1]**, **Yeongjoon Lee [2]**, **Woonghee Lee [2],\*** and **Chin-Ju Park [1],\***

[1] Department of Chemistry, Gwangju Institute of Science and Technology, Gwangju 61005, Korea; minjune1590@gm.gist.ac.kr (M.J.Y.); wlsdn8810@gist.ac.kr (J.K.)

[2] Department of Chemistry, University of Colorado Denver, Denver, CO 80217-3364, USA; bioyj1012@gmail.com

\* Correspondence: woonghee.lee@ucdenver.edu (W.L.); cjpark@gist.ac.kr (C.-J.P.); Tel.: +1-303-315-7672 (W.L.); +82-62-715-3630 (C.-J.P.)

**Abstract:** Proteins from *Sulfolobus solfataricus (S. solfataricus)*, an extremophile, are active even at high temperatures. The single-stranded DNA (ssDNA) binding protein of *S. solfataricus* (SsoSSB) is overexpressed to protect ssDNA during DNA metabolism. Although SsoSSB has the potential to be applied in various areas, its structural and ssDNA binding properties at high temperatures have not been studied. We present the solution structure, backbone dynamics, and ssDNA binding properties of SsoSSB at 50 °C. The overall structure is consistent with the structures previously studied at room temperature. However, the loop between the first two β sheets, which is flexible and is expected to undergo conformational change upon ssDNA binding, shows a difference from the ssDNA bound structure. The ssDNA binding ability was maintained at high temperature, but different interactions were observed depending on the temperature. Backbone dynamics at high temperature showed that the rigidity of the structured region was well maintained. The investigation of an N-terminal deletion mutant revealed that it is important for maintaining thermostability, structure, and ssDNA binding ability. The structural and dynamic properties of SsoSSB observed at high temperature can provide information on the behavior of proteins in thermophiles at the molecular level and guide the development of new experimental techniques.

**Keywords:** thermophile; thermostability; high temperature; OB-fold; single-stranded binding; NMR; backbone relaxation; solution structure; chemical shift perturbation; *Sulfolobus solfataricus*

## 1. Introduction

*Sulfolobus* is one of the well-known hyperthermophilic archaebacterial genera [1]. Unlike mesophilic eukaryotes and bacteria, which are sensitive to external conditions, *Sulfolobus* can survive at extremely low pH or high temperature [1–5]. *Sulfolobus solfataricus (S. solfataricus)* is adapted to high temperature via lipid composition changes [6], protection of its DNA with DNA binding proteins [7], and expression of a unique DNA topoisomerase [8]. Because they have the ability to survive in such harsh conditions, proteins from *S. solfataricus* are widely used in biological experiments and industrial applications that require low pH or high-temperature conditions [5]. Glyceraldehyde phosphate dehydrogenase, carboxypeptidase, alanine: glyoxylate transaminase, γ-lactamase, and other enzymes of *S. solfataricus* have been applied as industrial biocatalysts [9].

Single-stranded DNA (ssDNA) binding proteins (SSBs) of *S. solfataricus* are also used in biotechnological applications under harsh conditions. SSBs are proteins that bind to ssDNA non-sequence specifically. During the DNA replication or repair process, they prevent ssDNAs released by a helicase from returning to double-stranded DNAs (dsDNAs), and thereby increase the DNA polymerase activity. Thus, SSBs are essential for all living

organisms to preserve their genomes [10,11]. At high temperatures, dsDNAs substantially melt into ssDNAs, and ssDNAs are much more vulnerable to damage than dsDNAs [12]. Therefore, hyperthermophilic archaebacterial species, including *S. solfataricus*, that inhabit extremely hot environments, overexpress SSBs to protect single-stranded nucleic acids from severe conditions and retain their genes [13].

*S. solfataricus* SSB (SsoSSB) consists of 148 amino acids. The unbound structure determined using X-ray crystallography (PDB ID: 1O7I [14]) and the ssDNA bound structure determined at 25 °C using nuclear magnetic resonance (NMR) spectroscopy (PDB ID: 2MNA [15]) showed that the protein has a well-conserved oligonucleotide/oligosaccharide binding fold (OB-fold) domain. OB-folds consist of a well-conserved β barrel structure with five β strands capped by one α helix and an ssDNA binding pocket composed of $L_{12}$ and $L_{45}$ loops [16,17]. Human replication protein A (hRPA) [18], *Escherichia coli* SSB [19], and human mitochondrial SSB [20] are examples of SSBs that can bind to ssDNA strongly. Unlike other well-characterized SSBs, in which two aromatic residues are conserved and are important for ssDNA binding, SsoSSB has an extra aromatic residue (Figure 1), which increases the binding affinity for ssDNA by forming an additional π-π stacking interaction with ssDNA [13–15]. Although the structural properties of SsoSSB have been reported at room temperature, it remains unclear which structural and dynamic features are important for its high thermostability and ssDNA binding properties at the optimal survival temperature (55 to 88 °C [1–5]).
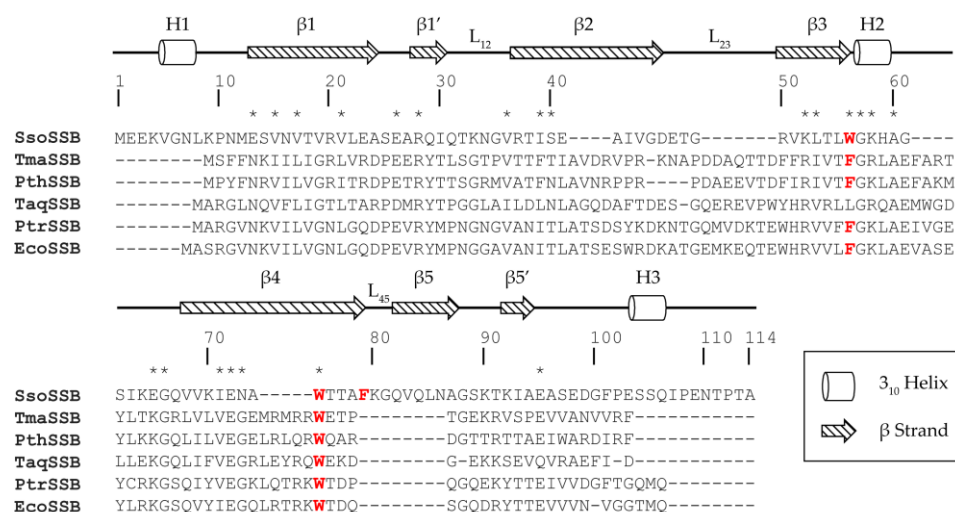


**Figure 1.** Sequence alignment of SsoSSB with SSBs from various bacteria: hyperthermophilic *Thermotoga maritima* (TmaSSB) and *Pseudothermotoga thermarum* (PthSSB); thermophilic *Thermus aquaticus* (TaqSSB), and *Pseudoalteromonas translucida* (PtrSSB); mesophilic *Escherichia coli* (EcoSSB). Conserved residues are indicated with an asterisk. Aromatic residues participating in base-stacking upon DNA binding are colored red. The secondary structure of SsoSSB from UniProt [21] and a previous study [14] are depicted above the sequence.

Here, we determined the structure of SsoSSB at high temperature (50 °C) using NMR spectroscopy. SsoSSB was shown to maintain a well-conserved OB-fold structure even at this high temperature, and its thermostability was measured using differential scanning calorimetry (DSC) and circular dichroism (CD) spectroscopy. The ssDNA binding activity and backbone dynamics of the protein were also investigated at high temperature using NMR spectroscopy. The spin relaxation experiments revealed that the protein surprisingly retained a highly rigid structure even at high temperature. Moreover, the protein was still able to interact with ssDNA at elevated temperatures. To determine the role of the N-terminal region in the thermostability and DNA binding of the protein, we analyzed the properties of an N-terminal deletion mutant using DSC, CD spectroscopy, isothermal titration calorimetry (ITC), and NMR. Our findings provide important understanding of

thermophilic SsoSSB near its physiological conditions and fundamental insights into its potential for biotechnological applications in high-temperature conditions.

## 2. Results

### 2.1. Thermostability of SsoSSB

SSBs have highly conserved sequences ranging from mesophiles to hyperthermophiles (Figure 1). Unlike other SSBs, SsoSSB has a unique N-terminal region containing an additional helix H1. All the individual secondary structure elements other than H1 and $\beta 5$ combine to form the well-conserved OB-fold structure. Compared with the canonical OB-fold structures, SsoSSB showed unique secondary structures (H1, $\beta 1'$, and $\beta 5'$) [14]. In addition to the highly conserved aromatic residues, W56 and W75, SsoSSB possesses an additional F79, which contributes to the increase in binding affinity for ssDNA by forming an additional base-stacking interaction [14].

To compare the thermostability of SsoSSB with other thermophilic SSBs, we performed DSC. From the DSC data, the melting temperature ($T_m$) of SsoSSB$_{1-114}$ was measured at 84.16 °C (Figure 2a), which is lower than that of the hyperthermophilic TmaSSB (109.3 °C) [22]. CD spectroscopy was performed at 20 °C to confirm the secondary structure of the protein (Figure S1a). There is a negative peak at 215 nm, which comes from $\beta$ strands [23], and a positive peak at 228 nm, which indicates $\beta$-II type $\beta$-rich protein [24,25]. We also monitored structural changes over the temperature range of 20 to 80 °C using CD. Molar ellipticity at 228 nm was plotted at intervals of 2 °C (Figure S1b). As the temperature increased from 20 to 80 °C, the molar ellipticity at 228 nm decreased by about 452,000 deg cm$^2$ dmol$^{-1}$. This suggests that the secondary structure became destabilized but not completely denatured [23–27]. When the temperature reached 80 °C, the sample was cooled to 20 °C to confirm whether SsoSSB$_{1-114}$ refolded after heating (Figure 2b). Our result showed that the CD spectrum was fully recovered, which implies that denaturation of the protein is reversible. This is consistent with the previous studies showing that the protein was not fully denatured, even at high temperatures, using $^1$H-$^{15}$N heteronuclear single-quantum coherence (HSQC) spectra [15,28].
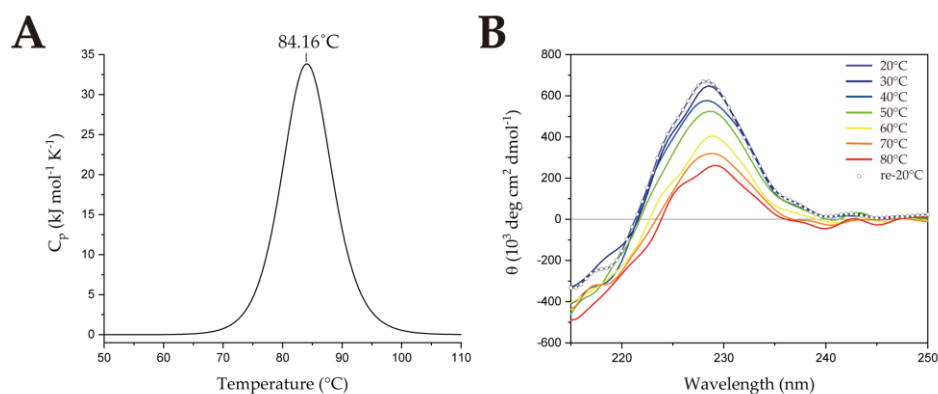


**Figure 2.** Thermostability of SsoSSB$_{1-114}$. (**A**) Melting temperature ($T_m$) of SsoSSB$_{1-114}$ measured by differential scanning calorimetry. (**B**) Circular dichroism spectroscopy was used to investigate the effect of temperature on the secondary structure of SsoSSB$_{1-114}$.

### 2.2. Solution Structure of SsoSSB$_{1-114}$ at High Temperature

We previously reported the backbone and sidechain atom chemical shift assignments of the protein at 50 °C (BMRB 50523) and presented 2D $^1$H-$^{15}$N HSQC spectra with the assignment [28]. To obtain high temperature distance constraints, nuclear Overhauser effects (NOEs) were observed from $^{15}$N- and $^{13}$C-edited-NOESY-HSQC experiments performed at 50 °C. The AUDANA algorithm [29] generated distance and torsion angle constraints using the protein sequence, chemical shift assignments, and NOESY data as inputs. TALOS-N [30]

and Xplor-NIH [31] operations were automated by AUDANA for torsion angle constraints and structure calculations, respectively.

We obtained 893 distance constraints from the NOESY data and 193 angle constraints from TALOS-N. In the previous study of the NMR structure at room temperature, 2294 intramolecular constraints were used for protein structure calculation [15]. It is known from previous studies that fewer constraints are measured at higher temperatures [32,33] because of various factors, including the partial denaturation of secondary structures and the reduced sensitivity at elevated temperatures. It was also found that there were relatively small numbers of medium-range constraints (85, 9.9% of total distance restraints) because the protein is mainly composed of β strands with a small amount of $3_{10}$ helical structure. For the structure calculation at room temperature, a similar proportion of medium-range restraints (8.5% of total distance restraints) was used [15]. The number of NOE constraints for each residue is shown in Figure S2.

The solution structure of the protein was calculated with Xplor-NIH in the PONDEROSA-C/S software package [34], starting from 100 random structures. The structural statistics are shown in Table 1. The 20 lowest energy models (Figure 3) were calculated with no violations and root-mean-square deviations (RMSDs) of 0.974 Å (backbone atoms) and 1.751 Å (heavy atoms). Ramachandran plot analysis from PROCHECK [35] revealed that all dihedral angles were within the allowed regions. The protein retained its secondary and tertiary structure at high temperature, containing five β strands and one $3_{10}$ helix (Figure 4a and Figure S3). Unstructured regions, especially the $L_{12}$ loop, residues 98–103, and the C-terminal region, were relatively not converged one another. The structure was deposited in the Protein Data Bank (PDB ID: 7WCG).

**Table 1.** Statistics of the solution structure of SsoSSB$_{1-114}$ at 50 °C. The 20 lowest energy structures were calculated using NMR restraints.

| Restraints [1] | | | Value |
|---|---|---|---|
| **Total NMR Constraints** | | | **1086** |
| | Distance Constraints | | |
| | | Intra Residue ( $\|i–j\| = 0$ ) | 259 |
| | | Sequential Residue ( $\|i–j\| = 1$ ) | 225 |
| | | Medium Range ( $1 < \|i–j\| \leq 5$ ) | 85 |
| | | Long Range ( $\|i–j\| > 5$ ) | 291 |
| | | Hydrogen Bond | 33 |
| | Dihedral Angle Constraints | | |
| | | Φ | 96 |
| | | Ψ | 97 |
| **Pairwise RMSD (Å) [2]** | | | |
| | Backbone Atoms [3] | | $0.974 \pm 0.044$ |
| | Heavy Atoms [3] | | $1.751 \pm 0.054$ |
| **Ramachandran Plot Summary from PROCHECK (%) [2]** | | | |
| | Most Favored Regions | | 94.9 |
| | Additionally Allowed Regions | | 3.9 |
| | Generously Allowed Regions | | 1.2 |
| | Disallowed Regions | | 0.0 |
| **wwPDB NMR Structure Validation [4]** | | | |
| | Clashscore | | 8 |
| | Ramachandran Outliers | | 2.0% |
| | Sidechain Outliers | | 1.0% |
| **Average Number of Violations Per Conformer [5]** | | | |
| | Distance Violations (>0.5 Å) | | 0 |
| | Angle Violations (>5°) | | 0 |

**Table 1.** *Cont.*

| Repulsive Violations | 0 |
|---|---|

[1] The solution structure of SsoSSB$_{1-114}$ was calculated using Xplor-NIH in PONDEROSA-C/S [36].
[2] The final 20 lowest energy structures were evaluated using Protein Structure Validation Software (PSVS) [35]. [3] Among ordered residues: E3-S97, S104-T113. [4] wwPDB (7WCG) validation results [37]. [5] Xplor-NIH pseudo-potential energy and every violation of the 20 best structures were analyzed using POKY-Analyzer [38].
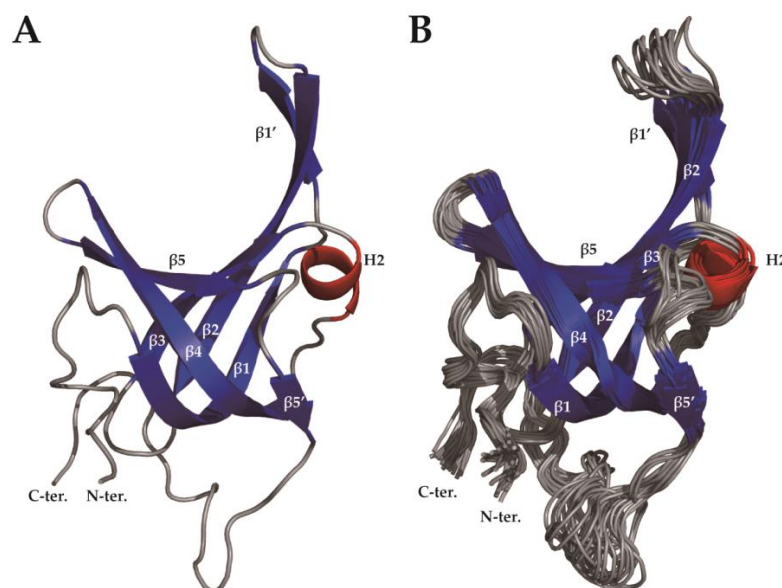


**Figure 3.** (**A**) The averaged 20 lowest energy solution structures of SsoSSB$_{1-114}$. (**B**) Ensemble of the 20 lowest energy solution structures of SsoSSB$_{1-114}$. The $3_{10}$ helix is indicated in red, and β strands are shown in blue.
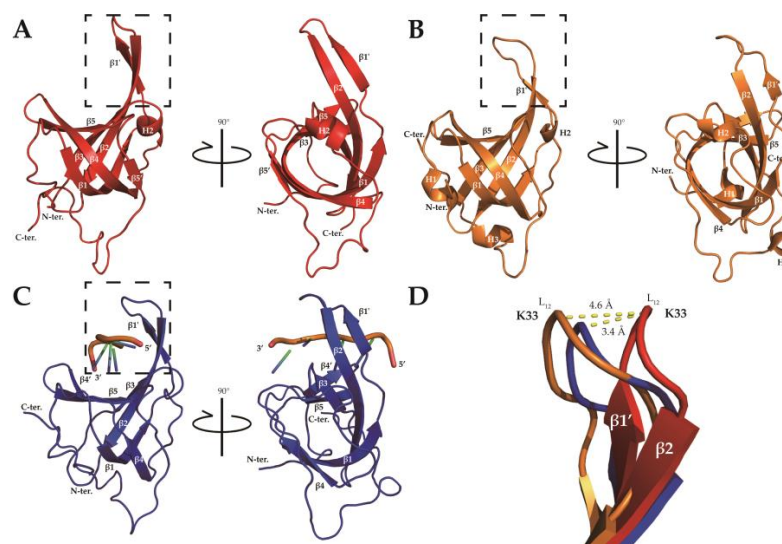


**Figure 4.** SsoSSB structures by (**A**) NMR at high temperature (PDB ID: 7WCG; indicated with red), (**B**) X-ray crystallography (PDB ID: 1O7I [14]; indicated with orange), and (**C**) NMR at room temperature in complex with ssDNA (PDB ID: 2MNA [15]; indicated with blue). (**D**) Magnified view of the L$_{12}$ loop in each of the 3 structures. The zoomed area is indicated by a dotted square in each figure (**A–C**).

It was already known that β strands β1, β4, and β5 are broken by residues 26, 72–73, and 89, respectively, which differs from the general OB-fold domain [14]. Secondary structure

prediction from the previous study suggested that SsoSSB$_{1–114}$ consists of nine β strands and three 3$_{10}$ helices [28]. The previous X-ray crystal structure (PDB ID: 1O7I) consisted of five β strands and three 3$_{10}$ helices, and the DNA-bound NMR structure at room temperature (25 °C) consisted of five β strands and two 3$_{10}$ helixes (Figure 4b,c and Figure S3). Most β strands were conserved in all structures. There were no 3$_{10}$ helices near the N- and C-termini in our calculated structure, leaving only the internal H2 helix. β strand β5′ was found only in the NMR structures and not in the X-ray structure. It is expected that these differences are partly due to the differences in the structure calculation methods of NMR and X-ray crystallography. The RMSD in the crystal structure (PDB ID: 1O7I) was calculated as 1.406 Å, and that in the solution structure at room temperature bound to ssDNA (PDB ID: 2MNA) was 1.954 Å.

Structural alignment of the three SsoSSB structures revealed that the L$_{12}$ loop in the high-temperature structure of SsoSSB highly deviates from the other two SsoSSB structures. Significant structure fluctuations in L$_{12}$ were also observed in the 20 ensemble structures (Figure 3b), implying that this loop region is highly flexible. This feature is consistent with the previous findings that L$_{12}$ was shown to be flexible from the asymmetric unit superimposition of the X-ray crystal structure [14] and the previous NMR study at room temperature [15]. The position of K33 α-carbon differed by 1.622 ± 0.985 Å (7WCG) and 0.507 ± 0.190 Å (2MNA), respectively. The L$_{12}$ loop, one of the regions forming the DNA binding pocket and that plays an important role in DNA binding of the OB-fold [14,16,17], is less converged at 7WCG than 2MNA. The position of the K33 α-carbon differed by 4.72 ± 1.61 Å (1O7I) and 3.88 ± 1.50 Å (2MNA), respectively. The position of the K33 α-carbon of lowest energy differed by 4.6 Å (1O7I) and 3.4 Å (2MNA), respectively (Figure 4d). L$_{12}$ of the crystal structure was bound to a sulfate ion, whereas L$_{12}$ of the room temperature NMR structure was bound to ssDNA. The high temperature structure confirmed that L$_{12}$ became more flexible and straightened because of the absence of its binding partner, ssDNA.

*2.3. SsoSSB$_{1–114}$–DNA Interaction at High Temperature by NMR CSP Analysis*

The Gamsjaeger group demonstrated that SsoSSB$_{1–114}$ binds to ssDNA at both room temperature and high temperature [15]. To obtain detailed DNA binding surfaces at the atomic level, we performed chemical shift perturbation (CSP) experiments with ssDNA at 25 °C and 50 °C (Figure 5). The average (standard deviation) CSP during ssDNA titration at 25 °C was 0.0763 (0.0928) ppm, and that at 50 °C was 0.0591 (0.0745) ppm. At 25 °C, residues V15, V19, Q31, T32, I39, W56 (sidechain atoms), F79, and Q84 were perturbed more than 1 standard deviation from the average, and residues I30, R37, S40, T54, W75 (sidechain atoms), and N86 were perturbed more than 2 standard deviations from the average. At 50 °C, residues V15, N34, R37, and I39 were perturbed more than 1 standard deviation from the average, and residues I30, Q31, T32, S40, T54, W75 (sidechain atoms), and F79 were perturbed more than 2 standard deviations from the average. Thus, the ssDNA binding sites and ssDNA binding interactions are similar at 25 °C and 50 °C. At the higher temperature, the perturbation of residues R37, Q84, and N86 was reduced, suggesting that the charged and polar interaction with ssDNA decreases at high temperature, and the hydrophobic interaction mainly remains. In the study from Kerr et al. [14], I30, W56, W75, and F79 were shown by alanine substitution to be important for ssDNA binding at 50 °C. Among these point mutants, the ssDNA binding affinity of W56A was reduced the most, but in our experiments, the sidechain of W56 did not interact with ssDNA at 50 °C (Figure 5b,d). It can be inferred from this that W56 indirectly affects the protein's ssDNA binding at 50 °C.
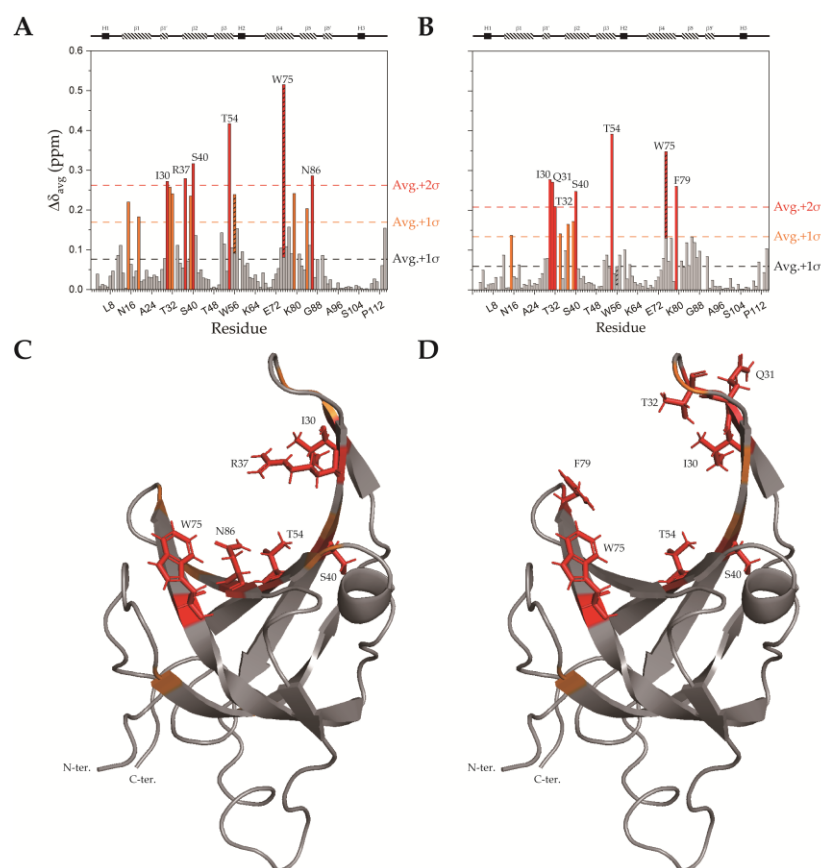
**Figure 5.** DNA binding site of SsoSSB$_{1-114}$. (**A**,**B**) Chemical shifts of $^{15}$N-labeled SsoSSB$_{1-114}$ at a concentration of 500 μM were perturbed upon ssDNA titration. Average CSP values ($\Delta\delta_{avg}$) for each residue of SsoSSB$_{1-114}$ with 1 mM ssDNA at (**A**) 25 °C and (**B**) 50 °C are shown. Trp sidechain CSPs are indicated with hatched bars. The secondary structure from UniProt is shown at the top of each graph. (**C**,**D**) The solution structure of SsoSSB$_{1-114}$ (PDB ID: 7WCG) was colored based on CSP data at (**C**) 25 °C and (**D**) 50 °C. Color coding is the same as in panels A and B. Sidechains are displayed for residues with the largest CSPs.

### 2.4. Backbone Dynamics of SsoSSB$_{1-114}$ at High Temperature and Room Temperature

To understand how the protein's backbone dynamics change with temperature, spin-lattice relaxation ($R_1$), spin-spin relaxation ($R_2$), and $^1$H-$^{15}$N heteronuclear Overhauser effect (hetNOE) experiments were performed at 25 °C and 50 °C. The average $R_1$ at 25 °C was $1.078 \pm 0.067$ Hz. Most residues had $R_1$ values within 2 standard deviations of the average. At 50 °C, the average $R_1$ value ($1.928 \pm 0.141$ Hz) was higher than that at 25 °C, and we found more deviations. This implies that the overall motion increases at 50 °C. Residues N34, G35, and V36 in loop $L_{12}$; residues S97 and E98 located in the loop between β5' and H3; residue N110 at the C-terminus had $R_1$ values > 2 standard deviations below the average (Figure 6a). Those regions have no secondary structural elements in 7WCG (Figure S3). In the X-ray crystal structure [14], $L_{12}$ and the region containing residues 94–100 were also found to be flexible. It is characteristic that the lower $R_1$ values were observed in a flexible region at 50 °C, unlike at 25 °C. Figure 6b shows the measured $R_2$ values of each residue at 25 °C and 50 °C. At 25 °C, the average $R_2$ value was $17.66 \pm 2.42$ Hz. Residues in loop $L_{12}$ and the C-terminal region showed reduced $R_2$ values, which indicate fast ps-ns dynamics [39]. At 50 °C, the average $R_2$ decreased significantly to $6.862 \pm 0.797$ Hz. This also suggests that the protein becomes more flexible at 50 °C. Residues that had reduced $R_1$ values at 50 °C also showed reduced $R_2$ values. From the $R_1$ and $R_2$ data, it was confirmed that the residues that experience fast dynamics were more prominent at 50 °C, and the overall motion of the protein was faster at a higher

temperature. From Figure 6c, we can observe higher $R_2/R_1$ values at 25 °C than 50 °C. The average tumbling time ($\tau_c$) values calculated from $R_2/R_1$ were 12.657 ns and 5.012 ns at 25 °C and 50 °C, respectively [40,41], indicating that the protein tumbles twice as fast at high temperature as it does at room temperature.
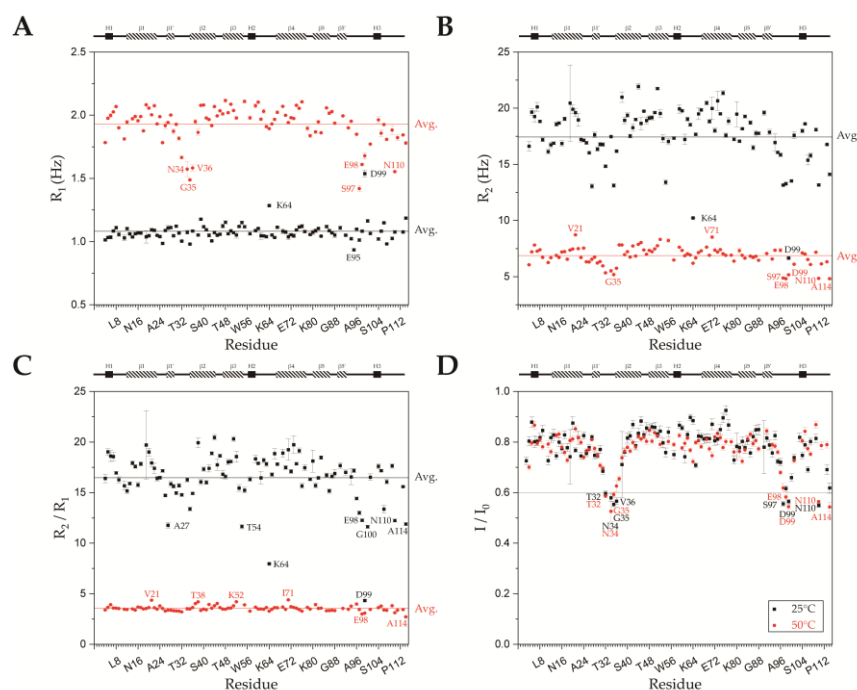


**Figure 6.** SsoSSB$_{1-114}$ backbone dynamics. Per residue (**A**) spin-lattice relaxation ($R_1$), (**B**) spin-spin relaxation ($R_2$), (**C**) $R_2/R_1$ ratios, and (**D**) hetNOE values at 25 °C and 50 °C are shown. Errors of the measurement are indicated by black and red lines. In panels A–C, average values of each parameter are indicated with a black (25 °C) or red (50 °C) line. Residues that differed from the average by more than 2 standard deviations are labeled. In panel (**D**), the hetNOE value 0.6 is indicated with a black line. Residues with values lower than 0.6 are labeled in black (25 °C) or red (50 °C). The secondary structure from UniProt is shown at the top of the graph.

From the hetNOE data (Figure 6d), residues T32, N34, G35, and V36 located in L$_{12}$; residues S97 and D99 in the loop between β5 and H3; N110 at the C-terminus had hetNOE values lower than 0.6 at 25 °C. Residues T32, N34, G35, E98, D99, N110, and A114 had hetNOE values lower than 0.6 at 50 °C. Thus, these regions are unstructured and more flexible, consistent with previous studies [14,15] and our $R_1$, $R_2$ relaxation experiments. The average hetNOE values were 0.780 and 0.766 at 25 °C and 50 °C, respectively, showing that the overall rigidity of the protein is maintained at 50 °C. Unlike the $R_1$ and $R_2$ values, the hetNOE values did not show a significant difference by temperature. Because the hetNOE value reflects the motion within the protein rather than the global motion of the protein within its chemical environment, this suggests that the internal motion of the protein is not changed much at increased temperatures [42].

### 2.5. Thermostability and ssDNA Binding Property of SsoSSB$_{12-114}$

It was already known that the helix between β3 and β4 in the OB-fold family is well conserved and makes a significant contribution to structural stabilization [17]. However, studies on the importance of the helix near the N-terminus are lacking. Because the N-terminal region of SsoSSB is not conserved among bacterial SSBs (Figure 1) and TmaSSB lacking this region has higher $T_m$ [22], we hypothesized the N-terminal region of SsoSSB is not crucial for the structural stabilization. The structure of SsoSSB (PDB ID: 7WCG) and TmaSSB (PDB ID: 1Z9F [43]) ss shown in the Supplementary Materials (Figure S4). To investigate the

role of the N-terminal region, an N-terminal deletion mutant (SsoSSB$_{12-114}$) was prepared. DSC was used to measure the T$_m$ value of SsoSSB$_{12-114}$ as 53.12 °C (Figure 7a). This was ~30 °C lower than the T$_m$ value of SsoSSB$_{1-114}$ and in a similar range to the mesophilic SSB, hRPA (70A subunit; 56.69 °C, Figure S5). CD spectroscopy was performed at 20 °C to confirm the secondary structure of the protein (Figure S1a). The overall pattern was very similar to SsoSSB$_{1-114}$, except that lower molar ellipticities were observed at 215 nm and 228 nm. The molar ellipticity was not fully recovered after heating and cooling (Figure 7b). Unlike the SsoSSB$_{1-114}$, molar ellipticity at 228 nm also changed significantly between 50 °C and 60 °C (Figure S1b). This is consistent with the DSC data. Together, these findings imply that SsoSSB$_{12-114}$ entirely loses thermostability. To monitor the structural changes that occur upon deletion of the N-terminal helix, we performed an $^1$H-$^{15}$N HSQC experiment on SsoSSB$_{12-114}$ at 25 °C (Figure S6a). The NMR spectra showed that the structure was not disordered, but when comparing the $^1$H-$^{15}$N HSQCs of SsoSSB$_{1-114}$ and SsoSSB$_{12-114}$, we observed that more than half of the peaks shifted due to the N-terminal deletion (Figure S6b).
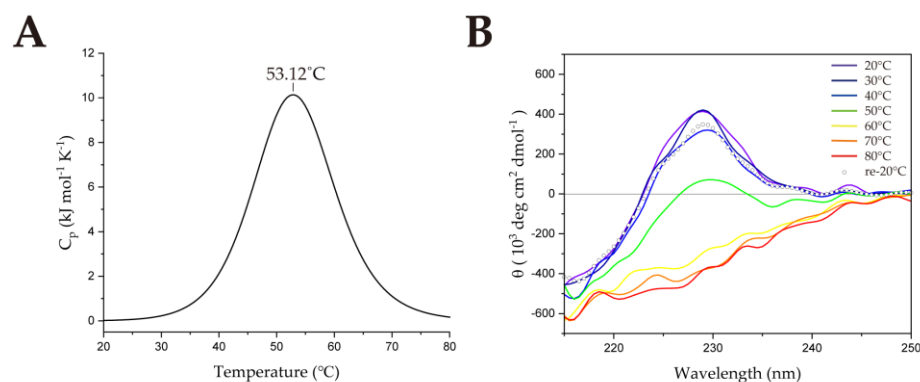


**Figure 7.** Thermostability of SsoSSB$_{12-114}$. (**A**) Melting temperature of SsoSSB$_{12-114}$ measured by differential scanning calorimetry. (**B**) Circular dichroism spectroscopy was used to investigate the effect of temperature on the secondary structure of SsoSSB$_{12-114}$.

A DNA titration was performed to see if SsoSSB$_{12-114}$ could still interact with ssDNA. There were some chemical shift changes observed due to the added ssDNA (Figure S6c). ITC experiments were also performed to measure the binding affinity. The dissociation constant (K$_d$) and stoichiometry (n) of SsoSSB$_{1-114}$ in the presence of dA(15) were 1.75 μM and 1.009 (Figure S7a), respectively, but we did not observe enough heat from the interaction of SsoSSB$_{12-114}$ and dA(15) to determine thermodynamic parameters (Figure S7b). Taken together, the deletion of the N-terminal 11 amino acids from SsoSSB dramatically affected its thermostability, structure, and DNA binding capability.

## 3. Discussion

In this study, we investigated the solution structure, DNA binding properties, and dynamic properties of the thermophilic SsoSSB at high temperature (50 °C). While the protein contains a well-conserved OB-fold domain and its structural aspects were already studied at room temperature [14,15], the structural and dynamic origins of thermophilicity were still not clearly understood. In this study, we collected NMR data to analyze the structure and backbone dynamics at 50 °C. We believe that this approach provides unique information to understand this thermophilic protein.

It is usually considered that a sufficient number of NOE (i.e., 10–20 NOEs per residue) are required for the reliable protein NMR structure calculation [44]. However, a recent study showed that the restraints per residue do not guarantee the accuracy of the structure. At the same time, Ramachandran analysis could be considered the accuracy indicator of the NMR structures [45]. While we used a relatively low number of NOE on average, we could collect a substantial number of long-range NOE using AUDANA algorithms for

the structure calculation. The structural statistics (Table 1) showed that our structure is acceptable and reflects the protein's nature.

Overall, our solution structure was similar to the previously described structures, while local differences in $L_{12}$ were revealed (Figure 8a–c). It is assumed that these differences were caused by the conformational change upon ssDNA binding, and that the flexibility of the region could contribute to the differences. Similar conformational differences were observed in hRPA70A, a eukaryotic OB-fold protein. The X-ray crystal structure of the apo form of hRPA70A (PDB ID: 1FGU [46]) and the ssDNA bound form of hRPA70A (PDB ID: 1JMC [47]) showed that the $L_{12}$ gets closer to the DNA and has a 'closed' conformation in the presence of ssDNA (Figure 8d–f). In the apo versus the DNA-bound form, the α carbon of S215, located at the top of $L_{12}$, shifts by 6.8 Å (Figure 8f), which is larger than the equivalent difference in SsoSSB (3.4 Å). In this regard, we suggest that our solution structure at high temperature represents the apo form of SsoSSB under near physiological conditions.
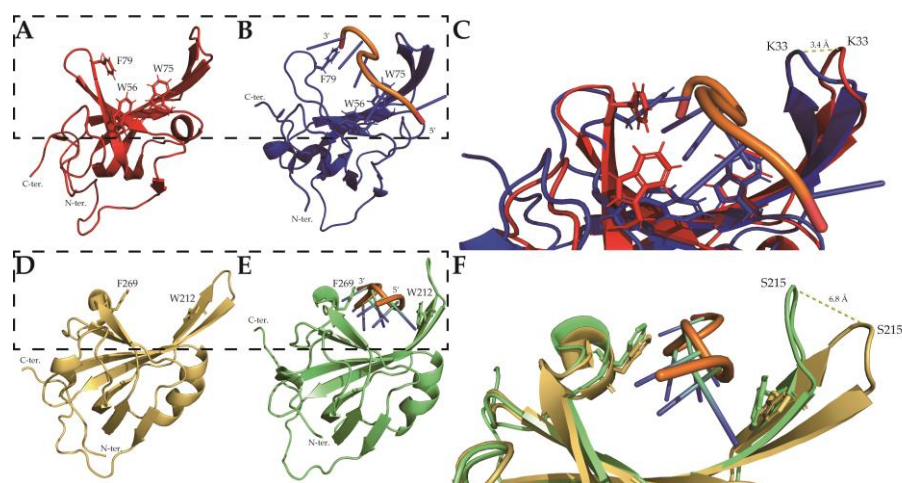


**Figure 8.** Protein structures of OB-fold proteins apo form and ssDNA bound form. NMR structure of SsoSSB (**A**) apo form (PDB ID: 7WCG; indicated with red) and (**B**) with ssDNA (PDB ID: 2MNA [15]; indicated with blue). (**C**) Zoom of the structure overlapping of (**A**,**B**). X-ray structure of hRPA70A (**D**) apo form (PDB ID: 1FGU [46]; indicated with yellow-orange) and (**E**) with ssDNA (PDB ID: 1JMC [47]; indicated with lime). (**F**) Zoom of the structure overlapping of (**D**,**E**). Aromatic residues which interact with ssDNA show with sidechain stick structure. The zoomed areas are indicated by a dotted square in each figure.

The aromatic residues involved in the stacking interaction with the DNA are shown in Figure 8a,b. Even though W56 is well conserved in bacterial SSBs (Figure 1), the structure showed that it contributes less than the other two residues (W75 and F79). This structure is consistent with our CSP analyses (Figure 5). Furthermore, we observed subtle differences in the DNA binding interface depending on the temperature. More electrostatic interactions were involved at room temperature, while hydrophobic interactions were more crucial at high temperature. This suggests that the nonspecific DNA binding of SsoSSB is mediated by an optimal combination of noncovalent interactions depending on the environment.

Because protein backbone dynamics are not usually assessed at a high temperature, it is not easy to compare our data with others. At or near room temperature, regions with ps-ns dynamics usually have higher $R_1$ (reduced $T_1$) and lower $R_2$ (elevated $T_2$) values [40]. At 50 °C, we observed that the average $R_1$ increased and $R_2$ decreased compared to the values at 25 °C (Figure 6a,b). This could reflect the general physical phenomena of proteins: the overall motion increases with elevated temperature. This interpretation is consistent with the rotational correlation time at 50 °C, being shorter than that at 25 °C. Unlike at 25 °C, the per residue $R_1$ value at 50 °C showed that the flexible regions such as the $L_{12}$ loop and the C-terminus have lower $R_1$ value than average (Figure 6a). This might be related to

the shortened rotational correlation time at 50 °C. One of the possible explanations is that the $R_1$ of the flexible region decreases in the same way as $R_2$ under conditions where $\tau_c$ is faster than the value expected from the protein's molecular weight [48]. Remarkably, the per residue hetNOE values were similar at both temperatures. Our data clearly showed that the overall protein folding was well maintained even at 50 °C, consistent with our DSC and CD data.

Previous studies found that electrostatic and hydrophobic interactions play an essential role in the thermal stabilization of thermophilic proteins [49–53]. We discovered that the N-terminus (residues 1 to 11) of SsoSSB is important for maintaining thermostability, even though it is located at the terminus of the protein and is not conserved across bacterial SSBs. An N-terminal deletion caused $T_m$ to decrease ~30 °C. The absence of the N-terminus resulted in partial destabilization of the protein (Figure 7b), affecting thermostability (Figure 7a) and DNA binding interaction (Figure S7b). These large disruptions led us to speculate that the N-terminus might contribute to the stability of the protein by acting as the lid of the β-barrel of the OB-fold. Since the binding affinity to ssDNA was so significantly reduced due to the absence of the N-terminal sequence (Figure S7b), which does not directly interact with ssDNA, it is reasonable to propose that the presence of the N-terminus is essential for maintaining the tertiary structure. From point mutation studies of the *Thermotoga maritima* acyl carrier protein [49], the $T_m$ decreases significantly by removing particular noncovalent interactions, while the mutant had a similar structure. Our study showed a different way to modulate the thermostability of these proteins, namely by truncating a region that is not included in the core structure. Further studies of the deletion mutant and other point mutants are required to reveal the complete origins of the thermostability of SsoSSB.

Based on our current understanding of the important residues and regions for thermostability, it is expected that it will be possible to make proteins with improved thermostability. For decades, efforts to improve protein stability and thermostability by protein engineering have continued. Introducing new disulfide bonds [54,55], optimizing metal chelation sites [56], and amino acid substitutions [57,58] have been thoroughly researched. However, improving thermal stability requires a lot of time and money. Recently, several computational studies [59,60] have been used to overcome these difficulties in biological research. In addition, deep learning and machine learning techniques have been employed to improve protein stability and thermostability [60–62]. Our study provides detailed information on the structure and ssDNA interactions of SsoSSB at high temperature. This information can provide fundamental insights into SSoSSB's industrial applications, such as increasing polymerase chain reaction efficiency [63], detecting viral nucleic acid [64], and potentially increasing the stability of mRNA vaccines [65].

## 4. Materials and Methods

### 4.1. Protein Expression and Purification

SsoSSB$_{1–114}$ and SsoSSB$_{12–114}$ were cloned into a pET C-terminal TEV His6 cloning vector with BioBrick polycistronic restriction sites (9Bc) and transformed into BL21(DE3) cells. We cultivated cells for more than 12 h in 10 mL LB medium (25 g/L) with ampicillin (0.3 mM, final concentration) at 37 °C. Into 1 L of LB medium containing ampicillin, 15 mL of overnight cultured cells was poured. Cells were grown at 37 °C until the optical density at 600 nm reached 0.5–0.6, and then isopropyl β-D-1-thiogalactopyranoside was added to a final concentration of 0.5 mM. Cells were incubated for an additional 14–18 h at 18 °C. Cells were centrifuged for 15 min at 7500 rpm at 4 °C. For separating endogenous nucleic acids from protein, we used a high salt binding buffer (50 mM NaH$_2$PO$_4$, 2 M NaCl, pH 8.0) and a high salt wash buffer (50 mM NaH$_2$PO$_4$, 2 M NaCl, 40 mM imidazole, pH 8.0). Cells were resuspended and sonicated in the high salt binding buffer. The sample was centrifuged for 15 min at 13,000 rpm, 4 °C, and the supernatant put into an Ni-NTA column (Cytiva, Marlborough, MA, USA). The high salt wash buffer and an elution buffer (50 mM NaH$_2$PO$_4$, 300 mM NaCl, 300 mM imidazole pH 8.0) were used sequentially to purify

the proteins. The proteins were further purified by gel filtration chromatography using a Hi-Load 16/600 75 pg column (Cytiva, Marlborough, MA, USA) with buffer A (100 mM NaCl, 20 mM 2-(N-morpholino)ethanesulfonic acid (pH 6.5). For expression of $^{15}$N- and $^{13}$C-labeled protein, cells were grown in M9 minimum media that included $^{15}$NH$_4$Cl and $^{13}$C-D-Glucose (Cambridge Isotope Laboratories, Inc., Tewksbury, MA, USA) as nitrogen and carbon sources. The composition of M9 minimum media was 870 mL of distilled water, 1 g of $^{15}$NH$_4$Cl, 100 mL of M9 10X salt, 20 mL of 10% glucose ($^{13}$C-labeled) solution, 2 mL of 1 M MgSO$_4$ solution, 0.3 mL of 1 M CaCl$_2$ solution, 0.33 mL of vitamin solution, and 10 mL of trace metal solution.

### *4.2. NMR Experiments*

The $^{15}$N- and $^{13}$C-labeled SsoSSB$_{1-114}$ sample was dissolved to a final protein concentration of 0.5–1.2 mM with 10% D$_2$O in buffer A. A Bruker 900 MHz NMR spectrometer equipped with a cryogenic triple-resonance probe at the Korea Basic Science Institute (Ochang, Korea), Bruker AVANCE Neo 600 MHz spectrometers at GIST Central Research Facilities with a cryogenic triple-resonance probe (Gwangju, Korea), and an Agilent DD2 700 MHz NMR spectrometer at Gyeongsang National University (Jinju, Korea) were used to collect NMR spectra. Backbone and sidechain assignments were performed in previous studies [28,66]. $^{15}$N- and $^{13}$C-edited NOESY-HSQC were collected at 50 °C with 150 ms and 300 ms mixing times for structure calculation. In CSP experiments, ssDNA composed of 15 adenines (dA(15)) was added at molar ratios ranging from 0:1 to 2:1 to $^{15}$N-labeled SsoSSB$_{1-114}$. Average CSP values ($\Delta\delta_{avg}$) were calculated using the following equation

$$\Delta\delta_{avg} = \sqrt{(\frac{\Delta\delta N}{5.88})^2 + (\Delta\delta H)^2} \qquad (1)$$

### *4.3. Solution Structure Calculation*

The 3D structure of SsoSSB$_{1-114}$ at 50 °C was calculated using Xplore-NIH-based computations in the PONDEROSA-C/S package [35], and NOE assignments were performed using NMRFAM-Sparky [37]. Following that, the 20 lowest energy structures were determined. PONDEROSA-Analyzer software [67] was used to assess and refine all angle and distance violations of the best 20 constructions. PSVS [36] was used to analyze the final 20 lowest energy structures. PyMOL (http://www.pymol.org, accessed on 8 March 2022) was used to create the protein structural diagrams and align the protein structures. The NOE constraints and final coordinates were deposited in the RCSB PDB under the accession number 7WCG (BMRB ID: 50523).

### *4.4. NMR Backbone Relaxation Experiment*

$R_1$ and $R_2$ of $^{15}$N, and $^1$H-$^{15}$N hetNOE data, were recorded on the Bruker AVANCE Neo 600 MHz spectrometers at GIST Central Research Facilities with cryogenic triple-resonance probes (Gwangju, Korea). Pseudo-3D NMR spectra were collected with relaxation delays of 20, 60, 100, 200, 400, 600, 800, 1000, 1200, and 1600 ms at 25 °C and 50 °C for the $^{15}$N $R_1$ measurements, and with relaxation delays of 16.96, 33.92, 67.84, 101.76, 135.68, 203.52, 271.36, 339.2, 407.04, and 547.72 ms at 25 °C and 50 °C for the $^{15}$N $R_2$ measurements. POKY was used to extract the relaxation rate constants by fitting the decay of peak height as a function of the relaxation delay to a single exponential function [38]. For the hetNOE measurement, interleaved 2D $^1$H-$^{15}$N HSQC spectra were acquired with and without an initial proton saturation of 2.5 s at 25 °C and 50 °C. hetNOE values were obtained from the ratios of peak heights between pairs of spectra, calculated with a POKY script [38]. For more accurate analysis, overlapping peaks were excluded from the data. The rotational correlation time ($\tau_c$) was calculated by this equation [39,40]

$$\tau_c = (\frac{1}{4\pi\nu_N})\sqrt{(6\frac{R_2}{R_1} - 7)} \qquad (2)$$

where $\nu_N$ is the resonance frequency of $^{15}$N in Hz.

### 4.5. Differential Scanning Calorimetry

The $T_m$s of SsoSSB$_{1-114}$, SsoSSB$_{12-114}$, and hRPA70A were measured by DSC using a NanoDSC system (TA instruments, New Castle, DE, USA). The protein samples were prepared at concentrations of 5 mg/mL in buffer A. The thermograms were recorded as the temperature was increased at a rate of 1 °C/min from 50 °C to 110 °C (SsoSSB$_{1-114}$) or 20 °C to 80 °C (SsoSSB$_{12-114}$ and hRPA70A). The pressure was kept constant at 3 atm to prevent evaporation of the solvent. Individual component peaks were resolved from the complex profiles after polynomial baseline correction, and the two-state scaled curve fittings were performed by the NanoAnalyze software (TA Instrument, New Castle, DE, USA).

### 4.6. Circular Dichroism Spectroscopy

The secondary structure of SsoSSB at various temperatures was assessed by far-UV CD experiments using a J-815 spectropolarimeter (Jasco, Tokyo, Japan). It was measured under two different conditions. A 100 μM protein sample was dissolved in buffer B (20 mM NaHPO$_4$, pH 6.5) and placed in a cuvette with a 0.2 mm path length. CD spectra were measured from 190 to 250 nm at 0.5 nm intervals at 20 °C. A 50 μM protein sample was dissolved in buffer A and placed in a cuvette with a 1 mm path length. CD spectra were measured from 210 to 250 nm at 0.5 nm intervals. The temperature was increased from 20 to 80 °C in 2 °C increments. After heating, the temperatures were decreased from 80 °C to 20 °C in 5 °C decrements. Every measurement was performed after waiting for 1 min between temperature changes. Temperature-dependent ellipticity changes at 228 nm were observed to monitor the heat denaturation of the protein. θ was calculated as described in previous papers [23,25–27].

### 4.7. Isothermal Titration Calorimetry

ITC experiments were carried out in buffer A with a Nano-ITC SV instrument (TA Instruments, New Castle, DE, USA). Twenty-four aliquots of 10 μL of 500 μM dA(15) were titrated at 25 °C into 50 μM of SsoSSB$_{1-114}$ and SsoSSB$_{12-114}$. The stirring speed was 300 rpm, and the interval between titrations was 250 s. The dissociation constant ($K_d$) and stoichiometry (n) were calculated by fitting to the independent model in the NanoAnalyze software (TA Instruments, New Castle, DE, USA).

**Abbreviations**

| | |
|---|---|
| CSP | chemical shift perturbation |
| CD | circular dichroism |
| DSC | differential scanning calorimetry |
| dA(15) | single-stranded DNA composed of 15 adenines |
| dsDNA | double-stranded DNA |
| hetNOE | heteronuclear Overhauser Effect |
| HSQC | heteronuclear single-quantum coherence |
| ITC | isothermal titration calorimetry |
| NMR | nuclear magnetic resonance |
| NOE | nuclear Overhauser effect |
| OB-fold | oligonucleotide/oligosaccharide binding fold domain |
| PDB | protein data bank |
| RMSD | root-mean-square deviation |
| $R_1$ | spin-lattice relaxation |
| $R_2$ | spin-spin relaxation |
| SSB | single-stranded DNA binding protein |
| ssDNA | single-stranded DNA |
| Sso | *Sulfolobus solfataricus* |
| $T_m$ | melting temperature |

**References**

1. Brock, T.D.; Brock, K.M.; Belly, R.T.; Weiss, R.L. *Sulfolobus*: A new genus of sulfur-oxidizing bacteria living at low pH and high temperature. *Arch. Mikrobiol.* **1972**, *84*, 54–68. [CrossRef] [PubMed]
2. Zillig, W.; Stetter, K.O.; Wunderl, S.; Schulz, W.; Priess, H.; Scholz, I. The *Sulfolobus*-"*Caldariella*" group: Taxonomy on the basis of the structure of DNA-dependent RNA polymerases. *Arch. Microbiol.* **1980**, *125*, 259–269. [CrossRef]
3. Grogan, D.; Palm, P.; Zillig, W. Isolate B12, which harbours a virus-like element, represents a new species of the archaebacterial genus *Sulfolobus*, *Sulfolobus shibatae*, sp. nov. *Arch. Microbiol.* **1990**, *154*, 594–599. [CrossRef] [PubMed]
4. Sakai, H.D.; Kurosawa, N. *Saccharolobus caldissimus* gen. nov., sp. nov., a facultatively anaerobic iron-reducing hyperthermophilic archaeon isolated from an acidic terrestrial hot spring, and reclassification of *Sulfolobus solfataricus* as *Saccharolobus solfataricus* comb. nov. and *Sulfolobus shibatae* as *Saccharolobus shibatae* comb. nov. *Int. J. Syst. Evol. Microbiol.* **2018**, *68*, 1271–1278.
5. Quehenberger, J.; Shen, L.; Albers, S.-V.; Siebers, B.; Spadiut, O. *Sulfolobus*–A potential key organism in future biotechnology. *Front. Microbiol.* **2017**, *8*, 2474. [CrossRef]
6. De Rosa, M.; Esposito, E.; Gambacorta, A.; Nicolaus, B.; Bu'Lock, J.D. Effects of temperature on ether lipid composition of *Caldariella acidophila*. *Phytochemistry* **1980**, *19*, 827–831. [CrossRef]
7. Guagliardi, A.; Napoli, A.; Rossi, M.; Ciaramella, M. Annealing of complementary DNA strands above the melting point of the duplex promoted by an archaeal protein. *J. Mol. Biol.* **1997**, *267*, 841–848. [CrossRef]
8. Forterre, P.; Bergerat, A.; Lopez-Garcia, P. The unique DNA topology and DNA topoisomerases of hyperthermophilic archaea. *FEMS Microbiol. Rev.* **1996**, *18*, 237–248. [CrossRef]
9. Littlechild, J.A. Archaeal enzymes and applications in industrial biocatalysts. *Archaea* **2015**, *2015*, 147671. [CrossRef]
10. Mushegian, A.R.; Koonin, E.V. A minimal gene set for cellular life derived by comparison of complete bacterial genomes. *Proc. Natl. Acad. Sci. USA* **2002**, *93*, 10268–10273. [CrossRef]
11. Ashton, N.W.; Bolderson, E.; Cubeddu, L.; O'Byrne, K.J.; Richard, D.J. Human single-stranded DNA binding proteins are essential for maintaining genomic stability. *BMC Mol. Biol.* **2013**, *14*, 9. [CrossRef] [PubMed]
12. Lindahl, T.; Nyberg, B. Rate of depurination of native deoxyribonucleic acid. *Biochemistry* **1972**, *11*, 3610–3618. [CrossRef] [PubMed]
13. Morten, M.J.; Gamsjaeger, R.; Cubeddu, L.; Kariawasam, R.; Peregrina, J.; Penedo, J.C.; White, M.F. High-affinity RNA binding by a hyperthermophilic single-stranded DNA-binding protein. *Extremophiles* **2017**, *21*, 369–379. [CrossRef] [PubMed]
14. Kerr, I.D.; Wadsworth, R.I.M.; Cubeddu, L.; Blankenfeldt, W.; Naismith, J.H.; White, M.F. Insights into ssDNA recognition by the OB fold from a structural and thermodynamic study of *Sulfolobus* SSB protein. *EMBO J.* **2003**, *22*, 2561–2570. [CrossRef]

15. Gamsjaeger, R.; Kariawasam, R.; Gimenez, A.X.; Touma, C.; Mcllwain, E.; Bernardo, R.E.; Shepherd, N.E.; Ataide, S.F.; Dong, Q.; Richard, D.J.; et al. The structural basis of DNA binding by the single-stranded DNA-binding protein from *Sulfolobus solfataricus*. *Biochem. J.* **2015**, *465*, 337–346. [CrossRef]

16. Murzin, A.G. OB(oligonucleotide/oligosaccharide binding)-fold: Common structural and functional solution for non-homologous sequences. *EMBO J.* **1993**, *12*, 861–867. [CrossRef]

17. Theobald, D.L.; Mitton-Fry, R.M.; Wuttke, D.S. Nucleic acid recognition by OB-fold proteins. *Annu. Rev. Biophys. Biomol. Struct.* **2003**, *32*, 115–133. [CrossRef]

18. Arunkumar, A.I.; Stauffer, M.E.; Bochkareva, E.; Bochkarev, A.; Chazin, W.J. Independent and coordinated functions of replication protein A tandem high affinity single-stranded DNA binding domains. *J. Biol. Chem.* **2003**, *278*, 41077–41082. [CrossRef]

19. Raghunathan, S.; Kozlov, A.G.; Lohman, T.M.; Waksman, G. Structure of the DNA binding domain of *E. coli* SSB bound to ssDNA. *Nat. Struct. Biol.* **2000**, *7*, 648–652. [CrossRef]

20. Qian, Y.; Johnson, K.A. The human mitochondrial single-stranded DNA-binding protein displays distinct kinetics and thermodynamics of DNA binding and exchange. *J. Biol. Chem.* **2017**, *292*, 13068–13084. [CrossRef]

21. The UniProt Consortium. UniProt: The universal protein knowledgebase in 2021. *Nucleic Acids Res.* **2021**, *49*, D480–D489. [CrossRef] [PubMed]

22. Olszewski, M.; Grot, A.; Wojciechowski, M.; Nowak, M.; Mickiewicz, M.; Kur, J. Characterization of exceptionally thermostable single-stranded DNA-binding proteins from *Thermotoga maritima* and *Thermotoga neapolitana*. *BMC Microbiol.* **2010**, *10*, 260. [CrossRef] [PubMed]

23. Greenfield, N.J. Using circular dichroism spectra to estimate protein secondary structure. *Nat. Protoc.* **2007**, *1*, 2876–2890. [CrossRef] [PubMed]

24. Fasman, G.D. *Circular Dichroism and Conformational Analysis of Biomolecules*; Plenum Press: New York, NY, USA, 1996; ISBN 978-03-0645-142-3.

25. Buchtova, M.; Chaloupkova, R.; Zakrzewska, M.; Vesela, I.; Cela, P.; Barathova, J.; Gudernova, I.; Zajickova, R.; Trantirek, L.; Martin, J.; et al. Instability restricts signaling of multiple fibroblast growth factors. *Cell. Mol. Life Sci.* **2015**, *72*, 2445–2459. [CrossRef]

26. Hider, R.C.; Kupryszewski, G.; Rekowski, P.; Lammek, B. Origin of the positive 225–230 nm circular dichroism band in proteins. Its application to conformational analysis. *Biophys. Chem.* **1988**, *31*, 45–51. [CrossRef]

27. Kelly, S.; Price, N. The use of circular dichroism in the investigation of protein structure and function. *Curr. Protein Pept. Sci.* **2005**, *1*, 349–384. [CrossRef]

28. Yang, M.J.; Lee, W.; Park, C.-J. Resonance assignments and secondary structure of thermophile single-stranded DNA binding protein from *Sulfolobus solfataricus* at 323K. *Biomol. NMR Assign.* **2021**, *15*, 159–164. [CrossRef]

29. Lee, W.; Petit, C.M.; Cornilescu, G.; Stark, J.L.; Markley, J.L. The AUDANA algorithm for automated protein 3D structure determination from NMR NOE data. *J. Biomol. NMR* **2016**, *65*, 51–57. [CrossRef]

30. Shen, Y.; Bax, A. Protein backbone and sidechain torsion angles predicted from NMR chemical shifts using artificial neural networks. *J. Biomol. NMR* **2013**, *56*, 227–241. [CrossRef]

31. Schwieters, C.D.; Bermejo, G.A.; Clore, G.M. Xplor-NIH for molecular structure determination from NMR and other data sources. *Protein Sci.* **2018**, *27*, 26–40. [CrossRef]

32. Kremer, W.; Schuler, B.; Harrieder, S.; Geyer, M.; Gronwald, W.; Welker, C.; Jaenicke, R.; Kalbitzer, H.R. Solution NMR structure of the cold-shock protein from the hyperthermophilic bacterium *Thermotoga maritima*. *Eur. J. Biochem.* **2001**, *268*, 2527–2539. [CrossRef] [PubMed]

33. Jung, A.; Bamann, C.; Kremer, W.; Kalbitzer, H.R.; Brunner, E. High-temperature solution NMR structure of TmCsp. *Protein Sci.* **2004**, *13*, 342–350. [CrossRef] [PubMed]

34. Lee, W.; Stark, J.L.; Markley, J.L. PONDEROSA-C/S: Client–server based software package for automated protein 3D structure determination. *J. Biomol. NMR* **2014**, *60*, 73–75. [CrossRef] [PubMed]

35. Bhattacharya, A.; Tejero, R.; Montelione, G.T. Evaluating protein structures determined by structural genomics consortia. *Proteins* **2007**, *66*, 778–795. [CrossRef]

36. Lee, W.; Tonelli, M.; Markley, J.L. NMRFAM-SPARKY: Enhanced software for biomolecular NMR spectroscopy. *Bioinformatics* **2015**, *31*, 1325–1327. [CrossRef]

37. Berman, H.; Henrick, K.; Nakamura, H. Announcing the worldwide Protein Data Bank. *Nat. Struct. Biol.* **2003**, *10*, 980. [CrossRef]

38. Lee, W.; Rahimi, M.; Lee, Y.; Chiu, A. POKY: A software suite for multidimensional NMR and 3D structure calculation of biomolecules. *Bioinformatics* **2021**, *37*, 3041–3042. [CrossRef]

39. de Medeiros, L.N.; Angeli, R.; Sarzedas, C.G.; Barreto-bergter, E.; Valente, A.P.; Kurtenbach, E.; Almeida, F.C.L. Backbone dynamics of the antifungal Psd1 pea defensin and its correlation with membrane interaction by NMR spectroscopy. *Biochim. Biophys. Acta* **2010**, *1798*, 105–113. [CrossRef]

40. Kay, L.E.; Torchia, D.A.; Bax, A. Backbone dynamics of proteins as studied by ^{15}N inverse detected heteronuclear NMR spectroscopy: Application to staphylococcal nuclease. *Biochemistry* **1989**, *28*, 8972–8979. [CrossRef]

41. Tremblay, M.-L.; Xu, L.; Sarker, M.; Liu, X.-Q.; Rainey, J.K. Characterizing aciniform silk repetitive domain backbone dynamics and hydrodynamic modularity. *Int. J. Mol. Sci.* **2016**, *17*, 1305. [CrossRef]

42. Baber, J.L.; Szabo, A.; Tjandra, N. Analysis of slow interdomain motion of macromolecules using NMR relaxation data. *J. Am. Chem. Soc.* **2001**, *123*, 3953–3959. [CrossRef] [PubMed]

43. DiDonato, M.; Krishna, S.S.; Schwarzenbacher, R.; McMullan, D.; Jaroszewski, L.; Miller, M.D.; Abdubek, P.; Agarwalla, S.; Ambing, E.; Axelrod, H.; et al. Crystal structure of a single-stranded DNA-binding protein (TM0604) from *Thermotoga maritima* at 2.60 Å resolution. *Proteins* **2006**, *63*, 256–260. [CrossRef] [PubMed]

44. Sugiki, T.; Kobayashi, N.; Fujiwara, T. Modern technologies of solution nuclear magnetic resonance spectroscopy for three-dimensional structure determination of proteins open avenues for life scientists. *Comput. Struct. Biotechnol. J.* **2017**, *15*, 328–339. [CrossRef] [PubMed]

45. Fowler, N.J.; Sljoka, A.; Williamson, M.P. A method for validating the accuracy of NMR protein structures. *Nat. Commun.* **2020**, *11*, 6321. [CrossRef] [PubMed]

46. Bochkareva, E.; Belegu, V.; Korolev, S.; Bochkarev, A. Structure of the major single-stranded DNA-binding domain of replication protein A suggests a dynamic mechanism for DNA binding. *EMBO J.* **2001**, *20*, 612–618. [CrossRef] [PubMed]

47. Bochkarev, A.; Pfuetzner, R.A.; Edwards, A.M.; Frappier, L. Structure of the single-stranded-DNA-binding domain of replication protein A bound to DNA. *Nature* **1997**, *385*, 176–181. [CrossRef] [PubMed]

48. Solomon, I. Relaxation processes in a system of two spins. *Phys. Rev.* **1955**, *99*, 559–565. [CrossRef]

49. Lee, Y.; Jang, A.; Jeong, M.-C.; Park, N.; Park, J.; Lee, W.C.; Cheong, C.; Kim, Y. Structural characterization of an ACP from *Thermotoga maritima*: Insights into hyperthermal adaptation. *Int. J. Mol. Sci.* **2020**, *21*, 2600. [CrossRef]

50. Brininger, C.; Spradlin, S.; Cobani, L.; Evilia, C. The more adaptive to change, the more likely you are to survive: Protein adaptation in extremophiles. *Semin. Cell Dev. Biol.* **2018**, *84*, 158–169. [CrossRef]

51. Hait, S.; Mallik, S.; Basu, S.; Kundu, S. Finding the generalized molecular principles of protein thermal stability. *Proteins* **2020**, *88*, 788–808. [CrossRef]

52. Fang, X.; Cui, Q.; Tong, Y.; Feng, Y.; Shan, L.; Huang, L.; Wang, J. A stabilizing alpha/beta-hydrophobic core greatly contributes to hyperthermostability of archaeal [P62A]Ssh10b. *Biochemistry* **2008**, *47*, 11212–11221. [CrossRef] [PubMed]

53. Tych, K.M.; Batchelor, M.; Hoffmann, T.; Wilson, M.C.; Hughes, M.L.; Paci, E.; Brockwell, D.J.; Dougan, L. Differential effects of hydrophobic core packing residues for thermodynamic and mechanical stability of a hyperthermophilic protein. *Langmuir* **2016**, *32*, 7392–7402. [CrossRef]

54. Perry, L.J.; Wetzel, R. Disulfide bond engineered into T4 lysozyme: Stabilization of the protein toward thermal inactivation. *Science* **1984**, *226*, 555–557. [CrossRef] [PubMed]

55. Gokhale, R.S.; Agarwalla, S.; Francis, V.S.; Santi, D.V.; Balaram, P. Thermal stabilization of thymidylate synthase by engineering two disulfide bridges across the dimer interface. *J. Mol. Biol.* **1994**, *235*, 89–94. [CrossRef]

56. Kellis, J.T.; Todd, R.J.; Arnold, F.H. Protein stabilization by engineered metal chelation. *Bio/Technology* **1991**, *9*, 994–995. [CrossRef]

57. Eijsink, V.G.H.; Vriend, G.; van der Vinne, B.; Hazes, B.; van den Burg, B.; Venema, G. Effects of changing the interaction between subdomains on the thermostability of *Bacillus* neutral proteases. *Proteins* **1992**, *14*, 224–236. [CrossRef]

58. Kwon, W.S.; Da Silva, N.A.; Kellis, J.T., Jr. Relationship between thermal stability, degradation rate and expression yield of barnase variants in the periplasm of *Escherichia coli*. *Protein Eng.* **1996**, *9*, 1197–1202. [CrossRef]

59. Wang, L.; Wang, H.-F.; Liu, S.-R.; Yan, X.; Song, K.-J. Predicting protein-protein interactions from matrix-based protein sequence using convolution neural network and feature-selective rotation forest. *Sci. Rep.* **2019**, *9*, 9848. [CrossRef]

60. Jia, L.; Yarlagadda, R.; Reed, C.C. Structure based thermostability prediction models for protein single point mutations with machine learning tools. *PLoS ONE* **2015**, *10*, e0138022. [CrossRef]

61. Feng, C.; Ma, Z.; Yang, D.; Li, X.; Zhang, J.; Li, Y. A method for prediction of thermophilic protein based on reduced amino acids and mixed features. *Front. Bioeng. Biotechnol.* **2020**, *8*, 285. [CrossRef]

62. Jia, L.-L.; Sun, T.-T.; Wang, Y.; Shen, Y. A machine learning study on the thermostability prediction of (R)-ω-selective amine transaminase from *Aspergillus terreus*. *Biomed. Res. Int.* **2021**, *2021*, 2593748. [CrossRef] [PubMed]

63. Dąbrowski, S.; Olszewski, M.; Piątek, R.; Kur, J. Novel thermostable ssDNA-binding proteins from *Thermus thermophilus* and *T. aquaticus*-expression and purification. *Protein Expr. Purif.* **2002**, *26*, 131–138. [CrossRef]

64. Kang, J.; Yeom, G.; Jang, H.; Oh, J.; Park, C.-J.; Kim, M.G. Development of replication protein A-Conjugated gold nanoparticles for highly sensitive detection of disease biomarkers. *Anal. Chem.* **2019**, *91*, 10001–10007. [CrossRef] [PubMed]

65. Uddin, M.N.; Roni, M.A. Challenges of storage and stability of mRNA-based COVID-19 vaccines. *Vaccines* **2021**, *9*, 1033. [CrossRef]

66. Gamsjaeger, R.; Kariawasam, R.; Touma, C.; Kwan, A.H.; White, M.F.; Cubeddu, L. Backbone and side-chain $^1$H, $^{13}$C and $^{15}$N resonance assignments of the OB domain of the single stranded DNA binding protein from *Sulfolobus solfataricus* and chemical shift mapping of the DNA-binding interface. *Biomol. NMR Assign.* **2014**, *8*, 243–246. [CrossRef]

67. Lee, W.; Cornilescu, G.; Dashti, H.; Eghbalnia, H.R.; Tonelli, M.; Westler, W.M.; Butcher, S.E.; Henzler-Wildman, K.A.; Markley, J.L. Integrative NMR for biomolecular research. *J. Biomol. NMR* **2016**, *64*, 307–332. [CrossRef]